Welding in the World (2025) 69:849–859
https://doi.org/10.1007/s40194-025-01935-5

RESEARCH PAPER

In situ alloying of AlCuSi using dual-wire-directed energy deposition with plasma

S. Reinbacher[1] · T. Klein[2] · C. Simson[2] · F. Warchomicka[1] · P. Spoerk-Erdely[1] · N. Enzinger[1]

Received: 1 October 2024 / Accepted: 6 January 2025 / Published online: 16 January 2025

Abstract

The current research explores additive manufacturing of a multi-phase material using dual-wire plasma-directed energy deposition technology. With this approach, new materials can be designed and tested easily on the basis of commercially available consumables. In this work, AlSi5 and CuAl8 solid wire consumables are used to produce a specific AlCuSi alloy by controlling the welding parameters and the wire feed ratio. Initial experimentation results in an alloy with 85.7 at.% aluminum, 8.4 at.% copper, 2.7 at.% silicon, and 3.2 at.% magnesium, but with some instabilities during the process. The presence of magnesium in the chemical composition could be related to plasma interaction with the substrate during the welding process. After optimizing the process parameters, the chemical composition obtained is about 76.3 at.% aluminum, 19.9 at.% copper, and 3.8 at.% silicon. Using microstructural analysis via light and scanning electron microscopy, defects such as pores and inadequately melted Cu wire material are observed in all materials produced. Although the optimization of the melting process improved the microstructure, it also increased the copper content, which in turn exerts a significant influence on the mechanical properties. Mechanical testing indicates significant embrittlement. The results underscore that the microstructure is heavily influenced by the chemical composition. Microstructural changes caused by the higher copper content, i.e., in particular the increase of the volume fraction of brittle intermetallic phases such as θ-Al_2Cu, result in severe embrittlement of the obtained materials, denoted by higher hardness and reduced toughness. We conclude that the use of dual-wire plasma additive manufacturing can develop new materials by in situ alloying.

Keywords AlCuSi alloy · Dual-wire plasma welding · Chemical composition · Al_2Cu phase · Microstructural analysis and mechanical testing

1 Introduction

AlCuSi alloys are composed of aluminum, copper, and silicon and result from advanced metallurgical developments aimed at optimizing performance. The study by Kim et al. [1] highlights the distinct phases that may prevail in AlCuSi samples as derived from the aluminum-rich region of the AlCuSi system (Fig. 1), specifically noting the contrast between the ductile α-Al phase, which enhances plasticity, and the brittle intermetallic Al_2Cu phase, which is responsible for good mechanical performance but leads to severe embrittlement when not properly embedded in the matrix microstructure. Research by Kim et al. [1] finds that bimodal eutectic matrix alloys, which include eutectics of varying length scales and morphologies, demonstrate superior properties. In a similar vein, Park et al. [2] report that a bimodal eutectic composition, featuring micrometer-sized binary eutectic colonies and a nanometer-sized ternary eutectic matrix, yields exceptional strength of 1 GPa and 11% plasticity at room temperature, aligning with Kim's findings of 773 MPa strength and 8% plasticity for the same alloy composition. Kim's analysis of 28 varied chemical compositions identifies a region in the ternary phase diagram [3] with high strength and plasticity, setting a target corridor for experimental pursuits where strength values exceed 730 MPa and fracture elongation over 8%. Kim et al. [1] specify that

Recommended for publication by Commission IX—Behaviour of Metals Subjected to Welding

✉ S. Reinbacher
stefan.reinbacher@student.tugraz.at

[1] Graz University of Technology – Institute of Material Science, Joining and Forming, 8010 Graz, Austria

[2] LKR Light Metals Technologies, AIT Austrian Institute of Technology, 5282 Ranshofen, Austria

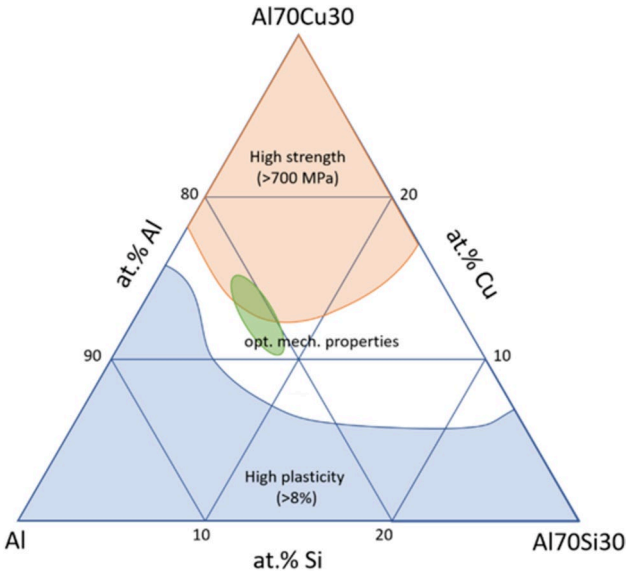

Fig. 1 The mechanical characteristic map of AlCuSi ultrafine eutectic composites superimposed on the AlCuSi ternary phase diagram in the Al-rich corner. According to [1]

samples numbered 12 to 17 in their work, with a chemical composition of 81–82 at.% aluminum, 15–17 at.% copper, and 4–7 at.% silicon, fall within this optimal range. This consideration leads to the central research question of whether similar results can be achieved using dual-wire plasma welding, specifically whether Kim's results based on electric arc melting combined with the rapid cooling sequence of suction casting can be replicated under additive manufacturing conditions.

Utilization of the direct energy deposition process presents both advantages and challenges. Among the advantages are the customized adaptation of alloy composition through the utilization of various materials for in situ alloying and the ability to efficiently manufacture components with different geometries. However, the process requires precise process control, rendering it highly complex in its application. This investigation aims to achieve a specific chemical composition by using dual-wire plasma-based additive manufacturing. One advantage of this process is the possibility of feeding two filler wires with different ratios to form a melt with the desired composition. Mechanical properties and microstructure of the material are evaluated to determine the relationship between process parameters, microstructure, and mechanical properties. This study provides a first insight into the development of new alloys on demand.

2 Materials and methods

The study on in situ alloying during additive manufacturing of AlCuSi samples was conducted using a plasma welding system which operates on the basis of an alternating current dual-wire technique [4–7]. The analysis of these samples included both mechanical and metallographic examinations.

2.1 Material

Two commercial filler materials with 1.2 mm diameter were selected to achieve the chemical composition of the deposited material. The selection of the commercial consumables was based only on availability and chemical composition. Table 1 shows the chemical composition of the filler materials AlSi5 and CuAl8, which contain the necessary elements for this study, as provided by the supplier. In addition, the results of energy-dispersive X-ray spectroscopy measurements of the major alloying elements are given in Table 1. A 7075 aluminum alloy served as the substrate for all experimental implementations due to material ability, with the relevant evaluation area established from the second layer onwards. It is assumed that this setup minimizes the influence of the base material on the chemical composition of the sample. Since for every commercially available base plate a certain mismatch in chemical composition was to be expected, we decided to use the 7075 Al plate based on its widespread availability. Three different batches were produced, each differing in their chemical composition.

2.2 Method

The plasma welding process was carried out with an M3DP-SL Scientific Line (SBI GmbH, Austria). This system allows the utilization of the principles of plasma hot-wire buildup welding, using two wires as additive material [10]. The wires are heated by a separate power source to near their

Table 1 Chemical composition of the filler wires used in this investigation according to the supplier and EDS

Filler wire		Element in wt.%							
		Al	Cu	Si	Mg	Fe	Mn	Zn	Ni
AlSi5	Nominal [8]	Base	< 0.3	4.5–6.0	< 0.2	< 0.6	< 0.1	< 0.1	-
	EDS	93.9		5.9		0.2			
CuAl8	Nominal [9]	8	Base	< 0.1	-	< 0.1	< 0.2	< 0.1	< 0.2
	EDS	8.3	91.7						

melting temperature to improve melting performance, stabilize the process, and control heat input, resulting in complete and clean melting of the wires by the plasma arc. The main advantage of this system is the use of separate sources for controlling the current in the plasma torch and the current for heating the wires, allowing adjustments in melt-off performance and material mixing. The wires are fed in a V-shape at an angle of approximately 30°. The wire feed speed for each wire can be controlled independently, permitting control of the materials input during welding. This scheme is shown in Fig. 2.

With this configuration, the objective was to produce samples with a chemical composition of 81–82 at.% aluminum, 15–17 at.% copper, and 4–7 at.% silicon. Since the feed rate ratio of the wires is a crucial precondition for achieving the target composition, iterative calculations based on filler wire composition lead to the determination of a wire feed rate ratio of $v_{\mathrm{AlSi5}} \approx 6.25 \times v_{\mathrm{CuAl8}}$ for two different wires with the same diameter, which results in a theoretical composition of 83 at.% aluminum, 12.7 at.% copper, and 4.3 at.% silicon.

The practical implementation of the welding experiments is divided into two phases: preliminary trials with the AlSi5 wire in a single-wire procedure to determine the suitable welding parameters and the production of three different batches by changing the current, welding speed, and wire feed speed of CuAl8 and AlSi5.

2.2.1 Welding trials

In *preliminary experiments*, welding parameters were explored using AlSi5 wire in a single-wire mode to develop optimal settings for subsequent dual-wire welding experiments. Wall structures measuring $22 \times 28 \times 100$ mm^3 were fabricated, consisting of three tracks in seven layers. The main current of 200 A was progressively reduced as the number of layers increased. The alternating current frequency and alternating current balance were set at 90 Hz and 75%, respectively. Wire feed occurred at a rate of 28 mm/s, welding speed was maintained at 4 mm/s, and the interlayer temperature was monitored and controlled at 150 °C using a pyrometer of the type Micro-Epsilon thermoMETER CTLaser.

In the *first batch*, gained through the dual-wire approach, the goal was to create suitable walls for follow-up characterization. In the first batch, three welding tracks were applied in five layers, resulting in a wall with dimensions of $64 \times 24 \times 100$ mm^3. The welding sequence and scheme are shown in Fig. 3, where numbers 1–15 represent the order of the individual tracks. The previously estimated feed rate ratio has to be adapted due to process instabilities to $v_{\mathrm{AlSi5}} \approx 6.25 \times v_{\mathrm{CuAl8}}$, which was leading to a wire feed speed of 50 mm/s for the AlSi5 wire and 8 mm/s for the CuAl8 wire. The variation in wire feed speeds is due to the initial use of a single-wire process with 28 mm/s as the baseline, followed by a transition to the two-wire process where 50 mm/s and 8 mm/s were optimized for quality and defect minimization. From the preliminary experiments, it also became evident that the AlSi5 wire is more manageable over a broader range of speeds. The limiting factor for a sound process and a homogeneous build is the CuAl8 wire. Due to its higher melting temperature and higher heat conductivity, it is quite challenging to add small amounts of liquid copper into the melt pool.

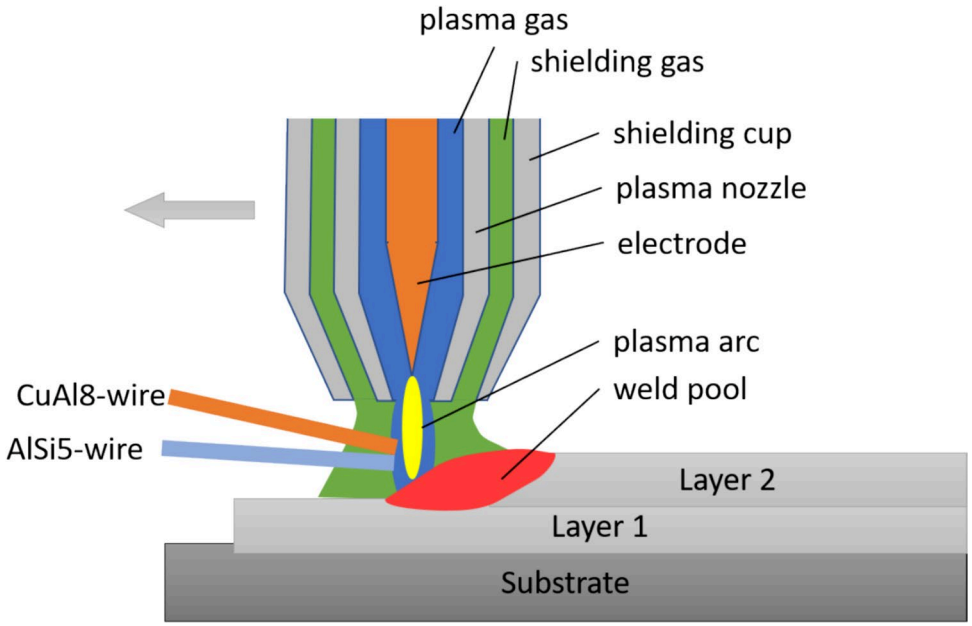

Fig. 2 Scheme of the dual-wire plasma welding system [11]

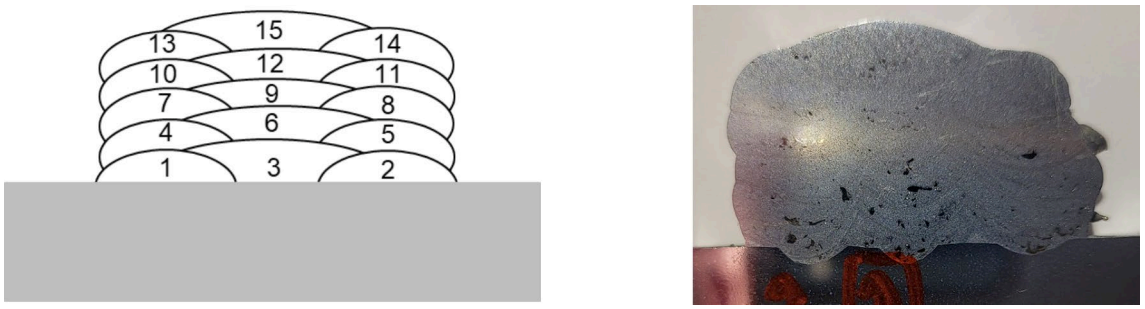

Fig. 3 Schematic building sequence (left) and real cross section (right)

Table 2 Parameters of batch 1

Layer	Main current [A]	Welding speed [mm/s]
1	250	1.5
2	225	1.725
3	212,5	1.725
4	200	1.8
5	200	1.95

This is why the AlSi5 wire was adjusted to match. The applied parameters are depicted in Table 2. The use of hot-wire technology at 45 A and control of the interlayer temperature to a maximum of 150 °C using a pyrometer is essential for the high energy input and the resulting challenges due to the increased temperatures. Particularly, the melting behavior of the CuAl8 wire is still not optimal at this ratio, due to its high melting temperature compared to the aluminum wire. This makes it necessary to weld more slowly compared with the results of the preliminary trials.

For the *second batch*, the main current was reduced to 200 A, and the welding speed was increased to 4 mm/s to lower the system temperature. Adjustments of the AC frequency to 58 Hz and the AC balance to 50% were also made. By increasing the feed rate of the CuAl8 wire and still controlling the interlayer temperature to a maximum of 150 °C using a pyrometer, the melting behavior of the wire improves by dripping evenly without melting back. This was achieved by adjusting the wire position within the plasma arc, enabling controlled heat input and mass transfer to the melt pool. In the second batch, a feed rate ratio of $v_{\mathrm{AlSi5}} \approx 3.7 \times v_{\mathrm{CuAl8}}$ was used, leading to a wire feed speed of 85 mm/s for the AlSi5 wire and 23 mm/s for the CuAl8 wire. A summary of these parameters is shown in Table 3. With these adjustments, a wall was produced with three tracks in five layers with dimensions of $40 \times 20 \times 100$ mm^3; however, it exhibits geometric defects primarily due to excessively high temperatures.

Table 3 Parameters of batch 2

Weld track number	Main current [A]	Welding speed [mm/s]	Hot-wire [A]
1, 2	200	4	25
3	200	3.2	45
4, 5	180	4.4	25
6	180	4.6	45
7, 8	180	4.4	25
9	180	4.6	45
10, 11	170	4.4	25
12	170	4.4	45
13, 14	160	4.4	25
15	160	4.2	45

Table 4 Parameters of batch 3

Weld track number	Main current [A]	Welding speed [mm/s]
1, 2, 4, 5, 7, 8, 10, 11, 13, 14	200	4
3, 6, 9, 12, 15	200	4.4

In the *third batch* of the experimental welding process, the general welding current was kept constant at 200 A, even with an increasing number of welding layers. The hot-wire current was significantly reduced from 45 to 10 amperes for all tracks, while the welding speed was only slightly increased to 4.4 mm/s. In this phase, the previously established feed rate ratio of $v_{\mathrm{AlSi5}} \approx 3.7 \times v_{\mathrm{CuAl8}}$ was reapplied. The interlayer temperature continued to be strictly monitored using a pyrometer and limited to a maximum of 150 °C (Table 4). The optimization of wire feeding into the plasma arc, a crucial step for the overall process, was continuously adjusted and improved through optical monitoring. The resulting structure of the wall consists of three welding tracks in five layers and has dimensions of $34 \times 22 \times 100$ mm^3. The parameter set for this third batch proves to be

reproducible and leads to no collapse of the wall. It is noteworthy that the feed rate ratio of batches 2 and 3 remains the same, and hence, theoretically, the chemical composition is macroscopically unchanged.

2.2.2 Characterization

For characterization, samples were taken from the produced walls. Tests for defects and heterogeneities after the welding process for all the batches were investigated by means of light optical microscopy (Zeiss Observer Z1M mat), while the microstructure of batches 1 and 3 and the fracture surface of Charpy samples (batch 3) were examined with a field emission gun scanning electron microscope (FEG-SEM) TESCAN MIRA3 with acceleration voltage between 10 and 20 kV, using a backscattered electrons (BSE) detector to identify the phases. The chemical composition along the height of the walls and the prevailing phases were determined with the aid of an Octane Super A C5 EDS detector (EDAX-Ametek). Acquisition and processing of the EDS measurements were performed with the APEX EDS software using 10 and 15 kV and a beam size of about 20 nm with an average measuring error of $6 \pm 2\%$. X-ray diffraction (XRD) was used for the crystallographic identification of prevailing phases. To this end, 4-mm-thick slices of walls taken from batch 1 were probed in transmission geometry at the Hereon-operated beamline P07B at PETRA III at the Deutsches Elektronen-Synchrotron (DESY) in Hamburg, Germany. High-energy X-ray diffraction patterns were recorded by means of a PerkinElmer XRD 1621 flat panel detector, using a mean photon energy of 87.1 keV and a beam size of 0.3×0.7 mm^2. The 2D patterns were azimuthally integrated with the aid of the software FIT2D [12]. Phase identification was conducted using the software MAUD [13, 14]. Mechanical testing was focused on batch 3, as this optimized batch showed the most stable repeatability. Charpy samples (DIN EN ISO 148–1:2017 [15]) were cut from the wall, horizontal to the welding direction. Due to the limited test volume available, only three tests at room temperature were performed with a Zwick pendulum impact tester (RKP450 model: BRA342038301; W_{nom}, 450 J). Furthermore, hardness measurements (HV0.5) along the building direction were carried out with the DuraScan 80 G5 machine. At least three measurements were performed for each distance from the substrate.

3 Results and discussion

3.1 Microstructure and defects

The microstructure of the first batch is examined using SEM images which are shown in Fig. 4. The SEM images reveal the presence of numerous pores, which is interpreted as a direct effect of the welding parameters used. Furthermore, due to the properties of CuAl8 wire and the process conditions, a notable presence of areas rich in copper is observed. This observation indicates inadequate assimilation of the copper wire into the melt pool during the DED process, as a direct consequence of the selected welding parameters and the physical properties of the wire. Since the same feedstock was used for all the experiments, it is very unlikely

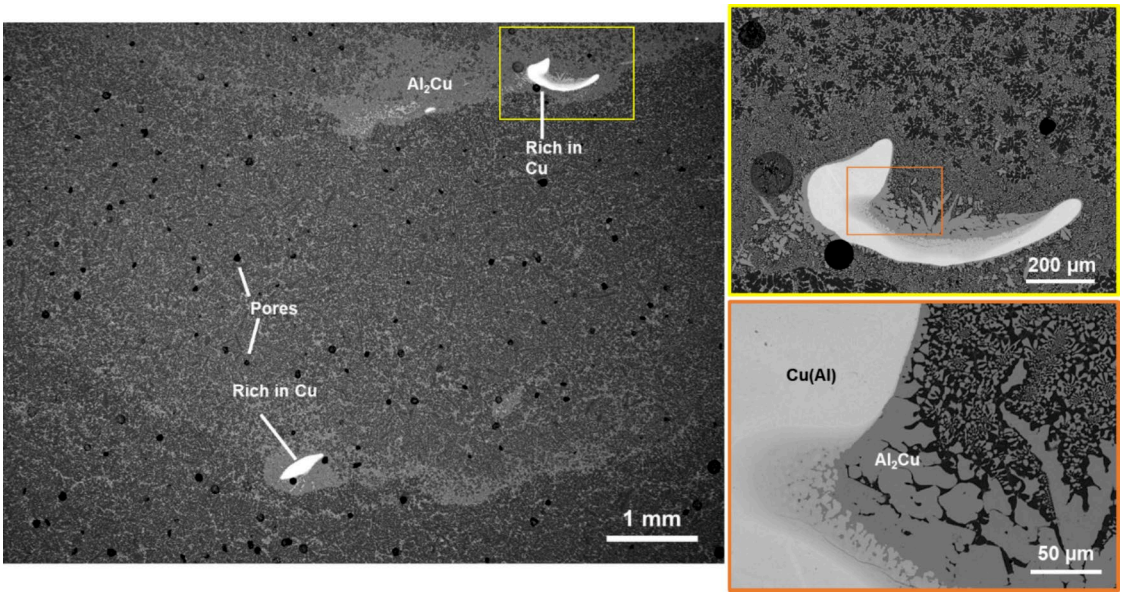

Fig. 4 SEM images of defects (pores and particles of Cu) and heterogeneities in the distribution of Al_2Cu in batch 1

that different levels of contamination should have caused changes in porosity. Changing process parameters led to a change in porosity, though. The particles with a high content of Cu worked as nucleation point for coarser Al_2Cu, with a high concentration of this phase observed at the bottom of the melt pool. The targeted chemical composition for batch 1 was 83 at.% Al, 14.7 at.% Cu, and 4.3 at.% Si, but EDS measurements revealed an average chemical composition of 85.7 at.% Al, 8.4 at.% Cu, 2.7 at.% Si, and 3.2 at.% Mg. The presence of magnesium in the chemical composition is due to the evaporation of this element from the substrate during the process. The chemical composition did not change significantly along the building height (Fig. 5). However, it can be observed that the magnesium content decreases with increasing height, which is attributed to dilution with the substrate. Conversely, a lower content of copper and silicon is observed at the bottom of the wall, which increases with height.

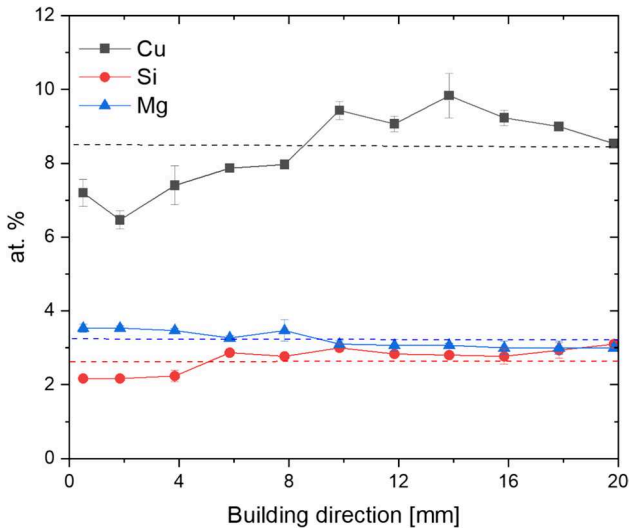

Fig. 5 Distribution of main alloying elements as a function of building height of batch 1 (left), batch 2 (middle), and batch 3 (right). Dashed lines represent the mean values for each element

The energy input during the DED process for the second batch is reduced by decreasing current and increasing welding speed, leading to a decrease in the overall system temperature and a more efficient energy distribution. This modification influences pore formation within the build component, resulting in smaller more finely distributed pores. It should be noted that this is purely a qualitative observation based on the images and has not been quantitatively analyzed.

Furthermore, the melting behavior of the CuAl8 wire had been optimized through adjustments in feed height, where both wires are fed into the plasma arc and not directly in the molten pool. One of the most significant changes in the welding parameter configuration is the adjustment of the feed rate ratio between the wire feeds. The ratio changed from $v_{AlSi5} \approx 6.25 \times v_{CuAl8}$ to $v_{AlSi5} \approx 3.7 \times v_{CuAl8}$. Due to this adjustment, the copper content increased from 8.4 at.% to values about 21 at.%. Although the copper content is increased compared with batch 1, copper accumulations within the material are significantly smaller than in the previous batch (Fig. 6).

Batch 2 exhibits a chemical composition of 74.6 at.% Al, 21.5 at.% Cu, and 4.0 at.% Si, leading to similar copper accumulations and pore sizes and distributions (Fig. 7). The chemical composition for batch 3 estimated by EDS is 76.2 at.% Al, 19.9 at.% Cu, and 3.8 at.% Si, close to the target composition. The chemical composition in building height was homogeneous, except for the first 4 mm of height with the presence of Mg from the substrate (Fig. 5).

The wall shows similar defects as batch 1, with areas rich in Cu, promoting the formation of coarser θ-Al_2Cu (Fig. 7). The distribution of θ-Al_2Cu seems to be more homogeneous along building height, but still with a higher concentration at the bottom of the molten pool.

3.2 Phase characterization

The microstructure of batch 1 shows primary α-Al dendrites, decorated mainly with Al_2Cu with different morphologies due to the cooling rate and thermal cycles

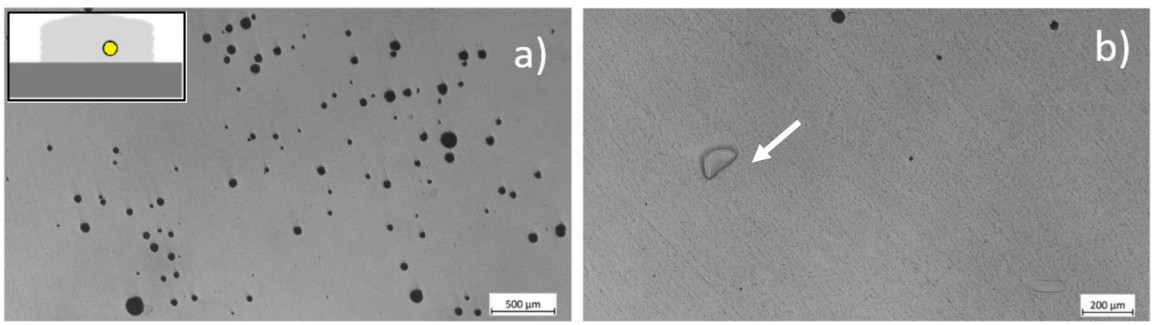

Fig. 6 Light optical microscopy of batch 2: **a** pores and **b** particle rich in copper

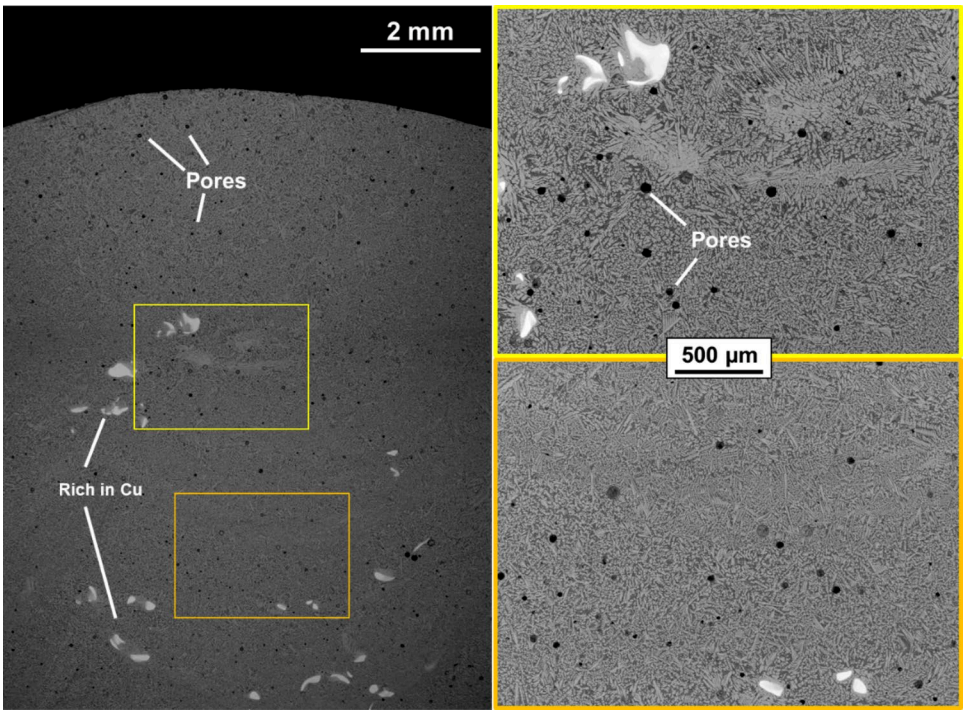

Fig. 7 SEM images of batch 3: defects (pores and particles of Cu) and distribution of Al_2Cu phase

during the process. Figure 8 illustrates the distribution of the main alloying elements in the microstructure, where the combination of elements in the microstructural features denotes more than two phases present in the material. Combining the results gained by means of SEM–EDS and XRD (Fig. 9a), four phases can be distinguished. The Al-rich phase could be identified as face-centered cubic α-Al phase (Fm3m structure). This phase appears in the shape of primary α dendrites (Fig. 8) as well as constituent of the eutectic matrix. Rietveld refinement of the XRD data showed that, in sum, the microstructure contains roughly 60 m.% of α phase at a representative measurement position located at the center of the wall slice. The bright Cu-rich phase represents θ-Al_2Cu (I4/

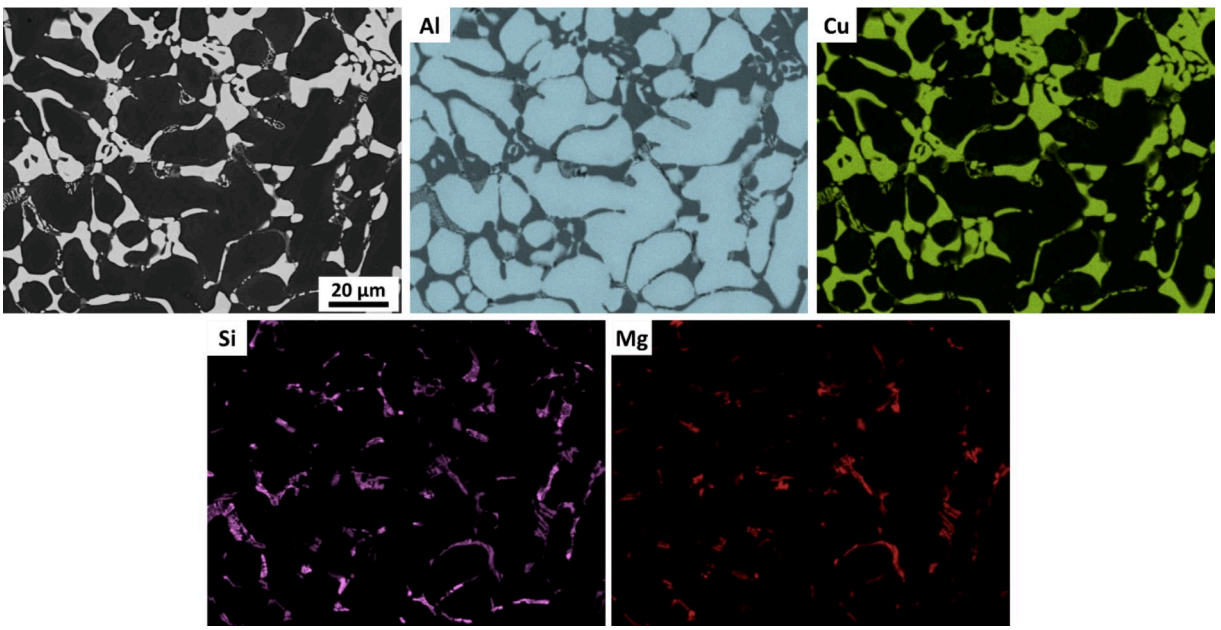

Fig. 8 Element distribution of representative area of batch 1

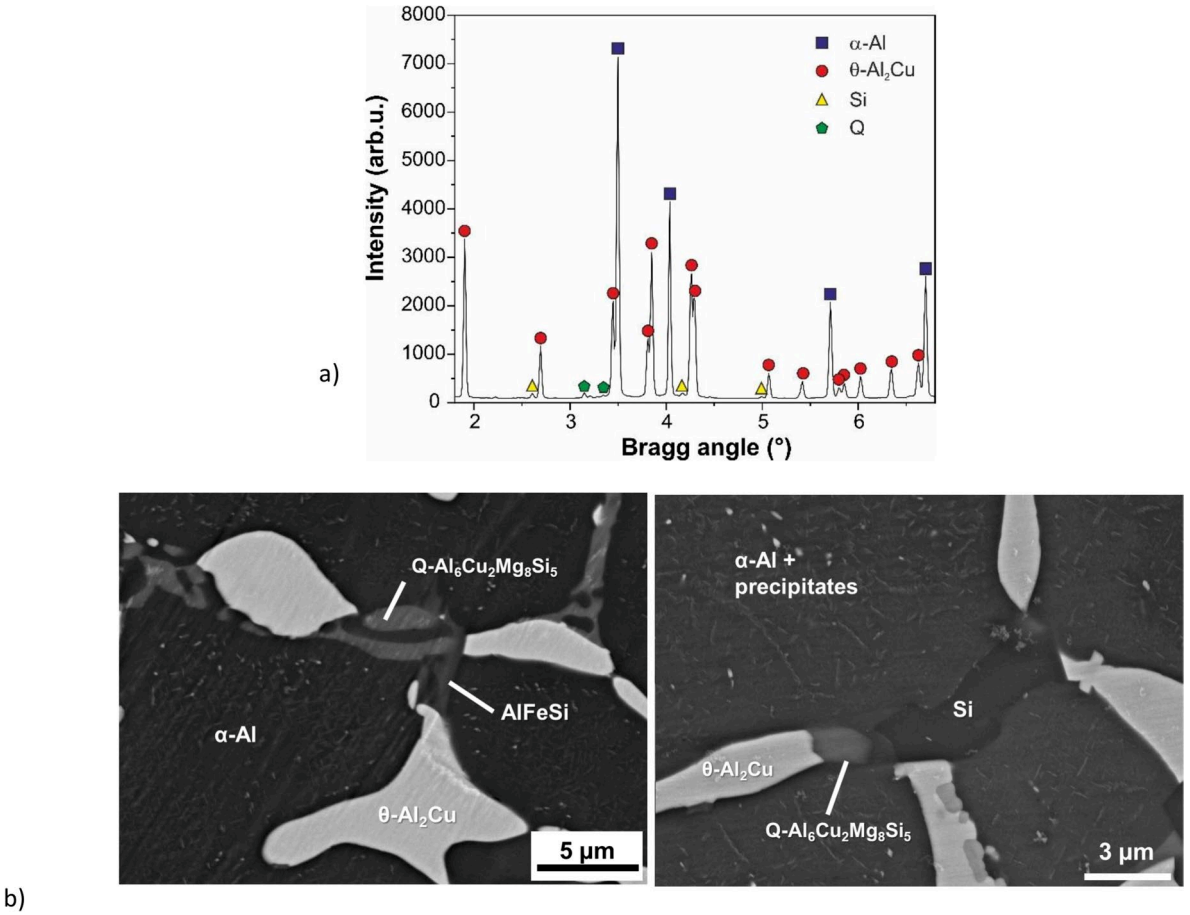

Fig. 9 **a** Azimuthally integrated XRD pattern recorded at a representative position within batch 1. **b** Identification of the phases in the microstructure by SEM–EDS measurements

mcm structure). At higher magnification (Fig. 9b), bright precipitates can also be distinguished within the α-Al grains, which likely also pertain to the θ phase. Rietveld refinement showed that roughly 40 m.% of θ-Al_2Cu is present in the microstructure. Furthermore, peaks pertaining to Si (Fd3m structure) as well as Mg-containing hexagonal Q-$Al_6Cu_2Mg_8Si_5$ phase were identified (Fig. 9) [16]. The fractions of these phases were found to be very small, though, falling below the quantification limit of the experimental technique of XRD. EDS measurements also found the presence of AlFeSi as part of the microstructure.

The microstructure of batch 3 shows a mostly dendritic structure of θ-Al_2Cu and also in eutectic form (Fig. 10) due to the high content of Cu in the chemical composition. EDS measurements determined not only the presence of θ-Al_2Cu and α-Al but also AlFeSi and Si particles. The presence of the iron-rich phase is likely due to the AlSi5 wire (see Table 1).

3.3 Hardness measurement

Hardness tests using the Vickers method (HV0.5) were conducted for all three batches along cross sections. Starting from the substrate, measurements were taken at set intervals up to the top layer to determine the hardness distribution (Fig. 11). Since the same substrate was used for all tests, the first measurements aligned to the substrate surface at 0 mm are approximately 80 HV for all cases. At a distance of approximately 10 mm from the first indentation site, which is in the second layer, the hardness levels remain similar. The second and third batches reach a maximum hardness of about 280 HV0.5. Since the first batch has a lower copper content, its average hardness levels are about 90 HV lower than those of the second and third batches. This investigation demonstrates that the resultant peak hardness is significantly influenced by the copper content in the material, which is in alignment with the results by Kim et al. [1]. While this adjustment in composition enhances hardness, it reduces the

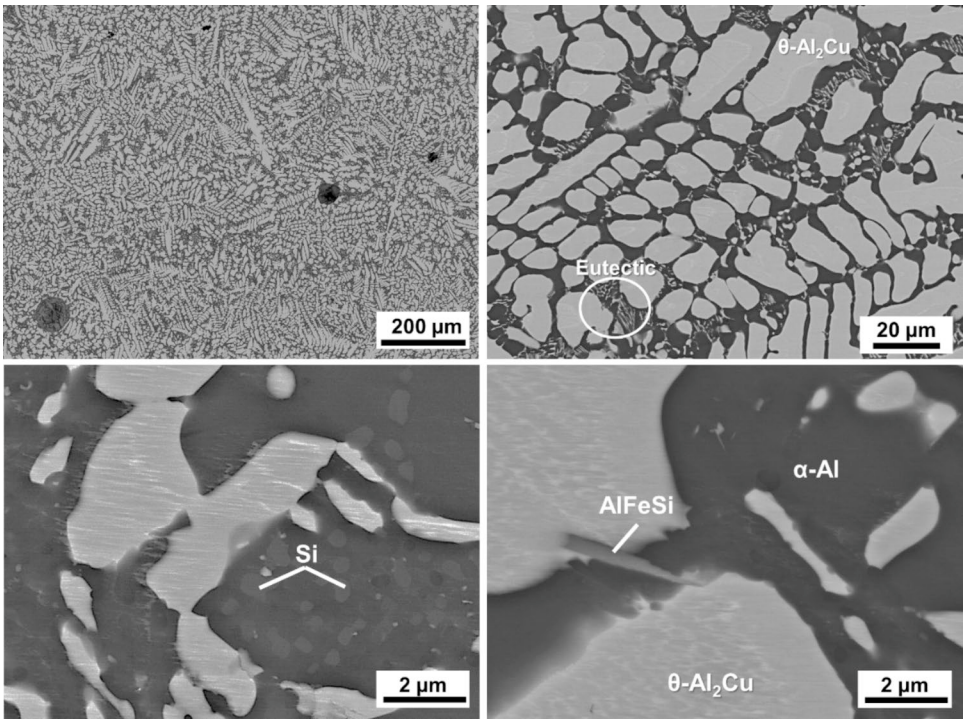

Fig. 10 Representative microstructure of batch 3 showing the distribution of the Al_2Cu phase and examples of Si and AlFeSi embedded in the α-Al matrix

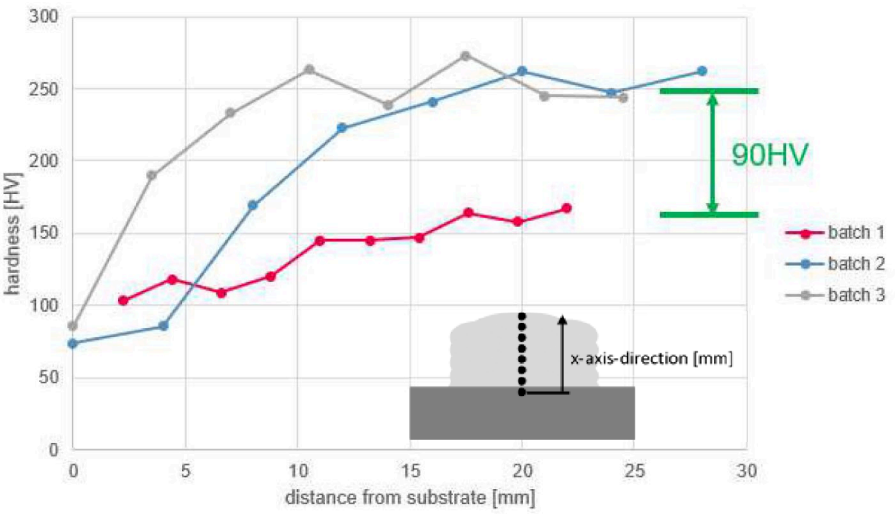

Fig. 11 Hardness test results of all three batches with HV0.5 Vickers

ductility of the material, primarily due to the brittle, primarily precipitated Al_2Cu phases [17, 18].

3.4 Charpy impact test

The impact energy for batch 3 was 1.8 ± 0.15 J, indicating that the material has practically no impact energy absorption. The fractured surface shows a brittle condition (Fig. 12), with almost no deformation due to the large amount of Al_2Cu present in the microstructure (Fig. 12c).

These observations suggest that the microstructural properties of the material, especially the presence of significant volume fractions of meso-scaled, primary dendritic Al_2Cu, play a significant role in reducing ductility and thereby compromising the toughness of the material. This emphasizes the need for careful consideration of alloy composition and microstructural characteristics in the development of materials intended for structural applications where both strength and ductility are critical [19].

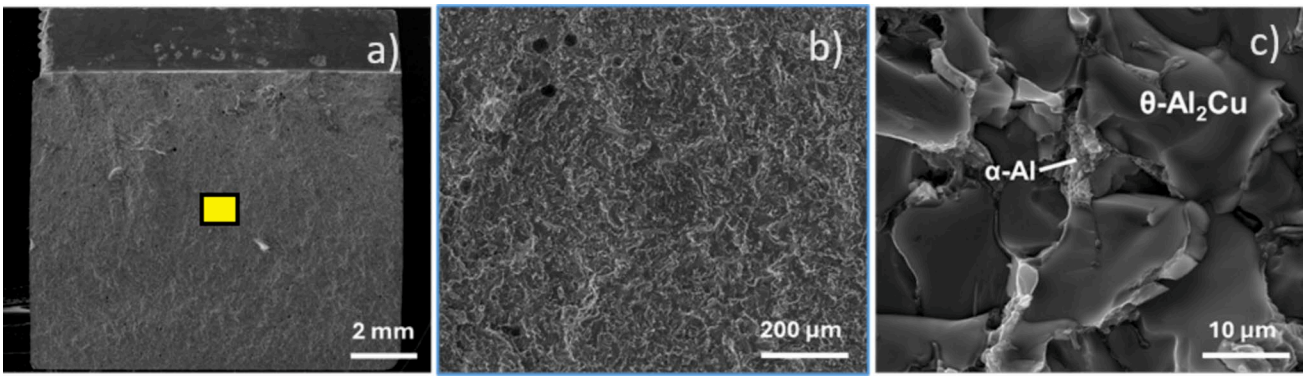

Fig. 12 **a**–**c** Fracture surface of Charpy sample of batch 3

4 Conclusions

This study shows the feasibility of in situ manufacturing of components using dual-wire plasma AM. The technique enables the production of a specific alloy by controlling the temperature and feed rate ratio of the filler materials. We produced three different batches with two chemical compositions of Al-Cu-Si, observing a large amount of θ-Al_2Cu phase embedded in an α-Al matrix.

Based on the findings presented in this paper, the following conclusions can be drawn:

1. The decoupled energy source and wire feedstock limit the stable process range, which leads either to large copper accumulations in the aluminum-rich matrix or alternatively to a higher copper content more equally dissolved in the bulk material.
2. The exact targeted chemical composition was not achieved, lying between the two realized compositions of batches 1 and 3.
3. All the studied batches showed additional Si and AlFeSi phases. The presence of Mg in batch 1 promoted the formation of the Q phase.
4. The batches with higher copper content show a clearly higher hardness. The presence and morphology of θ-Al_2Cu lead to a brittle behavior of the material.

Further optimization of the process will be essential to achieve more precisely the targeted composition with a homogenous microstructure. The selection of a proper substrate must be considered to avoid any additional modification of the target composition. The use of a copper consumable with a smaller diameter would help to achieve easily the expected composition. Additionally, thermal treatment is considered to modify the microstructural features to improve the mechanical properties.

Acknowledgements The consortium would like to thank the federal ministry for "Climate Action, Environment, Energy, Mobility, Innovation and Technology" (BMK), the ministry for "Digital and Economic Affairs" (BMDW), and the Austrian Funding Agency (FFG), as well as the four federal funding agencies Amt der Oberösterreichischen Landesregierung, Steirische Wirtschaftsförderungsgesellschaft m.b.H., Amt der Niederösterreichischen Landesregierung, and Wirtschaftsagentur Wien. Ein Fonds der Stadt Wien, for funding project "We3D" in the framework of the 7th COMET call.

We acknowledge DESY (Hamburg, Germany), a member of the Helmholtz Association HGF, for the provision of experimental facilities. Parts of this research were carried out at PETRA III, and we would like to thank N. Schell for assistance in using beamline P07B.

Funding Open access funding provided by Graz University of Technology. This research was funded by the Amt der Oberösterreichischen Landesregierung, Steirische Wirtschaftsförderungsgesellschaft m.b.H., Amt der Niederösterreichischen Landesregierung, and Wirtschaftsagentur Wien. Ein Fonds der Stadt Wien for funding project "We3D" in the framework of the 7th COMET call.

Declarations

Conflict of interest The authors declare no competing interests.

References

1. Kim JT, Lee SW, Hong SH et al (2016) Understanding the relationship between microstructure and mechanical properties of

Al-Cu-Si ultrafine eutectic composites. Mater Des 92:1038–1045. https://doi.org/10.1016/j.matdes.2015.12.080
2. Lee SW, Kim JT, Hong SH, et al (2014) Micro-to-nano-scale deformation mechanisms of a bimodal ultrafine eutectic composite. Sci Rep 1–5. https://doi.org/10.1038/srep06500
3. Raghavan V (2007) Al-Cu-Si (aluminum-copper-silicon) In: Journal of Phase Equilibria and Diffusion, pp 180–182. https://doi.org/10.1007/s11669-007-9024-y
4. Paul MJ, Klein T, Simson C et al (2022) Strength and fracture resistance of in-situ alloyed compositionally-graded Al-Si processed by dual-wire arc directed energy deposition. Addit Manuf 60:103291. https://doi.org/10.1016/J.ADDMA.2022.103291
5. Klein T, Paul MJ, Simson C et al (2022) Phase decomposition upon heat-treatment of a eutectoid Ti-Fe alloy processed by dual-wire-arc additive manufacturing. Mater Lett 319:132305. https://doi.org/10.1016/J.MATLET.2022.132305
6. Klein T, Birgmann A, Schnall M (2020) In situ alloying of aluminium-based alloys by (multi-)wire-arc additive manufacturing. MATEC Web of Conferences 326:01003. https://doi.org/10.1051/matecconf/202032601003
7. Eimer E, Suder W, Williams S, et al (2020) Wire laser arc additive manufacture of aluminium zinc alloys. In: Welding in the World, pp 1313–1319. https://doi.org/10.1007/s40194-020-00872-9
8. Böhler Welding (2017) Datenblatt UNION AL SI 5 Massivdraht. Available: https://voestalpine.com/welding. Accessed 5 June 2024
9. Rotek Handels GmbH (2008) MIG-WIG_CuAl8–2.0921. Available: https://media.rotek.at/aalg/schweissen/werkstoffe/MIG-WIG_CuAl8-2.0921_Datenblatt_Rotek_de.pdf. Accessed 5 June 2024
10. Motta MF, Santiago KG, Pessoa EF, et al (2020) Creating in-situ alloys by welding — new perspectives for advanced materials and applications. https://doi.org/10.1016/j.jmrt.2020.03.109
11. Wallis C, Neubauer E, Kitzmantel M et al (2023) Investigations of plasma metal deposition (PMD) of 6061 and 7075 aluminum alloys for aerospace and automotive applications. BHM Berg-Huettenmaenn Monatsh 168:209–218. https://doi.org/10.1007/s00501-023-01345-4
12. Hammersley AP, Svensson SO, Hanfland M et al (1996) Two-dimensional detector software: from real detector to idealised image or two-theta scan. High Press Res 14:235–248. https://doi.org/10.1080/08957959608201408
13. Lutterotti L, Chateigner D, Ferrari S, Ricote J (2004) Texture, residual stress and structural analysis of thin films using a combined X-ray analysis. Thin Solid Films 450:34–41. https://doi.org/10.1016/j.tsf.2003.10.150
14. Lutterotti L, Bortolotti M, Ischia G, et al (2007) Rietveld texture analysis from diffraction images. In: Tenth European Powder Diffraction Conference. Oldenbourg Wissenschaftsverlag, pp 125–130
15. DIN EN ISO 148–1:2017–05 (2017) Metallische Werkstoffe—Kerbschlagbiegeversuch nach Charpy—Teil 1: Prüfverfahren; CEN: Brussels, Belgium
16. Jianglong G, Jing B, Jialuo D, et al (2018) Design and cracking susceptibility of additively manufactured Al-Cu-Mg alloys with tandem wires and pulsed arc. https://doi.org/10.1016/j.jmatprotec.2018.06.030
17. Gupta A, Ling S (1999) Microstructure and mechanical properties of hypo/hyper-eutectic Al–Si alloys synthesized using a near-net shape forming technique. https://doi.org/10.1016/S0925-8388(99)00062-6
18. Geiger AL, Walker JA (1991) The processing and properties of discontinuously reinforced aluminum composites. https://doi.org/10.1007/BF03221097
19. Sjölander E, Seifeddine S (2010) The heat treatment of Al–Si–Cu–Mg casting alloys. https://doi.org/10.1016/j.jmatprotec.2010.03.020